

NEAR-EARTH ASTEROID SATELLITE SPINS UNDER SPIN–ORBIT COUPLING

SHANTANU P. NAIDU¹ AND JEAN-LUC MARGOT^{1,2}

¹ Department of Earth, Planetary, and Space Sciences, University of California, Los Angeles, CA 90095, USA

² Department of Physics and Astronomy, University of California, Los Angeles, CA 90095, USA

Received 2014 September 29; accepted 2014 November 4; published 2015 January 30

ABSTRACT

We develop a fourth-order numerical integrator to simulate the coupled spin and orbital motions of two rigid bodies having arbitrary mass distributions under the influence of their mutual gravitational potential. We simulate the dynamics of components in well-characterized binary and triple near-Earth asteroid systems and use surface of section plots to map the possible spin configurations of the satellites. For asynchronous satellites, the analysis reveals large regions of phase space where the spin state of the satellite is chaotic. For synchronous satellites, we show that libration amplitudes can reach detectable values even for moderately elongated shapes. The presence of chaotic regions in the phase space has important consequences for the evolution of binary asteroids. It may substantially increase spin synchronization timescales, explain the observed fraction of asynchronous binaries, delay BYORP-type evolution, and extend the lifetime of binaries. The variations in spin rate due to large librations also affect the analysis and interpretation of light curve and radar observations.

Key words: minor planets, asteroids: general – minor planets, asteroids: individual (2000 DP107, 1999 KW4, 2002 CE26, 2004 DC, 2003 YT1, Didymos, 1991 VH, 2001 SN263, 1994 CC, 1996 FG3) – planets and satellites: dynamical evolution and stability

1. INTRODUCTION

Binary near-Earth asteroids (NEAs) are numerous in the asteroid population. Both radar and light curve data have shown that ~16% of NEAs larger than ~200 m diameter have satellites (Pravec et al. 1999; Margot et al. 2002; Pravec et al. 2006). It is now widely accepted that binary NEAs form by a spin-up process (Margot et al. 2002) and that the specific spin-up mechanism is the YORP torque (Rubincam 2000). Binary NEA systems exhibit interesting post-fission and spin-orbit dynamics (e.g., Ostro et al. 2006; Scheeres et al. 2006; Fahnestock & Scheeres 2008; McMahon & Scheeres 2013) that profoundly affect their evolution (e.g., Jacobson & Scheeres 2011a; Fang & Margot 2012a; Jacobson et al. 2014), but the range of dynamical regimes has not been fully explored.

In this paper, we develop a method for simulating the coupled spin and orbital motions of two rigid bodies with arbitrary mass distributions. This technique is significantly faster than a similar implementation by Fahnestock & Scheeres (2006), because in our implementation the computationally expensive volume integrals over the two bodies are computed only once before the integration, as opposed to once per time step. We use our technique to perform a survey of the dynamics of all well-characterized binary NEA systems and map the range of dynamical behaviors, including the spin configurations of asteroid satellites. These results provide important insights for modeling the physical properties of binaries and for understanding the long term evolution of the binary systems.

The sample of well-characterized binaries includes all NEA systems with known estimates of system mass, semimajor axis, eccentricity, and component sizes. In practice, only systems observed with radar fall in this class. Over 35 binary NEAs have been observed with radar, but only about 10 have sufficient data to yield mutual orbits and component size estimates. We apply our technique to these systems.

Sections 2 and 3 describe the implementation of our coupled spin-orbit integrator and cover energy and angular momentum

conservation properties. Section 4 explains different kinds of satellite spin librations and sets up the notation used in subsequent sections. In Section 5, we examine the spin-orbit coupling effect and compare numerical and analytical estimates of libration amplitudes. Section 6 introduces surface of section plots which are used to identify resonant, chaotic, and non-resonant quasi-periodic trajectories. We examine the trajectories and spin configurations of satellites in well-characterized binary and triple NEA systems in Section 7 and show that large chaotic zones exist in the phase space of known asynchronous satellites. We also compute libration amplitudes for synchronous satellites. We discuss implications of the results in Section 8.

2. NUMERICAL INTEGRATION

We numerically investigate the coupled spin and orbital dynamics of two extended rigid objects under their mutual gravitational influence. We neglect the translational motion of the system barycenter and use the six first-order differential equations of motion (EOMs) derived by Maciejewski (1995). Here we express these EOMs in the body-fixed frame of the primary:

$$\begin{aligned} \dot{\mathbf{P}} &= \mathbf{P} \times \boldsymbol{\Omega}_1 - \frac{\partial V}{\partial \mathbf{R}}, & \dot{\mathbf{R}} &= \mathbf{R} \times \boldsymbol{\Omega}_1 + \frac{\mathbf{P}}{m}, \\ \dot{\boldsymbol{\Gamma}}_2 &= \boldsymbol{\Gamma}_2 \times \boldsymbol{\Omega}_1 + \boldsymbol{\mu}_2, & \dot{\boldsymbol{\Gamma}}_1 &= \boldsymbol{\Gamma}_1 \times \boldsymbol{\Omega}_1 + \boldsymbol{\mu}_1, \\ \dot{S} &= S\hat{\boldsymbol{\Omega}}_2 - \hat{\boldsymbol{\Omega}}_1 S, & \dot{S}_1 &= S_1\hat{\boldsymbol{\Omega}}_1. \end{aligned} \quad (1)$$

Here \mathbf{R} and \mathbf{P} are the relative position and linear momentum vectors of the secondary with respect to the primary, respectively, $m = m_p m_s / (m_p + m_s)$ is the reduced mass of the system, where m_p and m_s are the masses of the primary and secondary, respectively, V is the mutual gravitational potential, $\boldsymbol{\mu}$'s are the torque vectors acting on the two components, $\boldsymbol{\Omega}$'s are their angular velocity vectors, and $\boldsymbol{\Gamma}$'s are their angular momentum vectors. Subscripts 1 and 2 denote quantities that

refer to the primary and the secondary, respectively. Further, S and S_1 are attitude rotation matrices: the former mapping from the secondary frame to the primary frame, and the latter mapping from the primary frame to the inertial frame. A hat ($\hat{\cdot}$) symbol above a vector specifies an operator that maps a 3-vector (e.g., $\mathbf{v} = [v_x, v_y, v_z]$) to an antisymmetric 3×3 matrix, as follows:

$$\hat{\mathbf{v}} = \begin{bmatrix} 0 & -v_z & v_y \\ v_z & 0 & -v_x \\ -v_y & v_x & 0 \end{bmatrix}. \quad (2)$$

The term $\partial V/\partial \mathbf{R}$ is the gradient of the mutual gravitational potential, which is the gravitational force (vector) between the two components. All vectors in Equation (1) are expressed in the body-fixed frame of the primary. However, when computing $\hat{\Omega}_2$, one must express $\mathbf{\Omega}_2$ in the body-fixed frame of the secondary.

The gravitational force and torques are computed at each time step according to the method detailed in Ashenberg (2007). They are functions of \mathbf{R} , S , and the inertia integrals of the two bodies. The inertia integrals encode the mass distribution information of a body and are of the form:

$$I_{x^p y^q z^r} = \int_B x^p y^q z^r dm, \quad (3)$$

where dm is a mass element of body B at body-fixed coordinates (x, y, z) and the integral is a volume integral over the entire body. The body-fixed coordinate system is aligned with the principal axes and its origin is at the center of mass of B . The exponents p , q , and r are either 0 or positive integers, such that $p + q + r > 0$. We use inertia integrals up to fourth order in the integrations, where the order of an inertia integral is given by the sum of exponents, i.e., $p + q + r$. The inertia integrals depend only on the mass distribution of the object and remain constant throughout the integration, so we compute them only once before the integration. At each time step, current values of \mathbf{R} and S from the integrator are passed as arguments to the modules that compute force and torques.

Because detailed 3D shape models of both the primary and secondary are generally not available and their density distributions are unknown, we model the primary and secondary as triaxial ellipsoids (semi-axes a , b , and c) with uniform density in this paper. These restrictions can be easily lifted as knowledge progresses. The uniform-density ellipsoid assumption simplifies the computation of inertia integrals (Boué & Laskar 2009): they are zero for odd p , q , or r , and the non-zero integrals are simple functions of principal moments of inertia. The fourth-order inertia integrals can be found in Boué & Laskar (2009), and the non-zero second-order inertia integrals are listed below:

$$\begin{aligned} I_{x^2} &= \int x^2 dm = \frac{(-A + B + C)}{2}, \\ I_{y^2} &= \int y^2 dm = \frac{(A - B + C)}{2}, \\ I_{z^2} &= \int z^2 dm = \frac{(A + B - C)}{2}. \end{aligned} \quad (4)$$

Here, $A \leq B \leq C$ are the principal moments of inertia of the object about the x , y , and z axes, respectively.

We use the Cash–Karp method (Cash & Karp 1990) to integrate Equation (1). It is a fifth-order Runge–Kutta

integrator with adaptive stepsize control which uses an embedded fourth-order Runge–Kutta formula to compute errors. We use the implementation provided by Press et al. (1992) and set the fractional error tolerance to 10^{-15} .

In all simulations, we assume a planar system, i.e., both bodies are in principal axis rotation about their z (shortest) axes and their equatorial planes are aligned with the mutual orbit at all times. We start all simulations at the pericenter of the osculating mutual orbit and with the longest axis of each body pointing toward each other. The system parameters and initial osculating mutual orbital parameters for all simulations are given in Table 1.

3. ENERGY AND ANGULAR MOMENTUM CONSERVATION

In this section, we describe results of tests designed to evaluate the energy and angular momentum conservation properties of the integrator. Figure 1 illustrates a representative test run with the parameters given in the first line of Table 1. For this test case, we used triaxial ellipsoids with principal axis half-lengths of $a = 600$, $b = 500$, and $c = 400$ m for the primary, and $a = 252$, $b = 229$, $c = 190$ m for the secondary. The initial spin periods of the primary and the secondary are 2.775 hr and 32.59 hr, respectively.

The total energy is conserved at a level of $10^{-2} \text{ J yr}^{-1}$, which is about 10^{-11} times the mean orbital energy and less than 10^{-8} times the magnitude of the energy exchanged between the binary components and the mutual orbit.

Angular momentum is conserved at a level of $220 \text{ kg m}^2 \text{ s}^{-1}$ per year, which is less than 10^{-11} times the total angular momentum of the system ($\sim 10^{14} \text{ kg m}^2 \text{ s}^{-1}$) and less than 10^{-8} times the angular momentum exchanged between the component spins and the mutual orbit.

4. NOTATION AND LIBRATION CONCEPTS

Figure 2 illustrates the various angles used throughout the paper. θ is the angle between the secondary’s long axis and the line of apsides of the the osculating mutual orbit, and $\dot{\theta}$ is its time rate of change. If the apsidal precession rate were zero, $\dot{\theta}$ would correspond to the spin rate of the satellite. The instantaneous values at pericenter are denoted with a subscript p : θ_p , $\dot{\theta}_p$. The angle θ is related to the angle between the satellite’s long axis and the primary–secondary line, α , by $\theta + \alpha = f$, where f is the true anomaly of the mutual orbit. At pericenter, $f = 0$, so $\theta_p = -\alpha$.

Oscillations of the secondary orientation with respect to the primary-to-secondary line are called *librations*. In order to illustrate librations, let us first examine a situation in which the amount of angular momentum exchanged between the spin of the secondary and the mutual orbit is negligible. In this situation, we can treat the spin and orbit to be decoupled. A common approach to analyze the spin of the secondary is to assume the secondary to be a triaxial ellipsoid on a fixed Kelperian mutual orbit about a spherical primary. The secondary spin is affected by the gravitational torques exerted by the primary (e.g., Murray & Dermott 1999). In this situation, the angle α is the sum of *free*, *forced*, and *optical* libration angles. *Free libration* is easiest to understand in the case of a circular mutual orbit and a synchronously spinning secondary, i.e., a secondary whose average spin rate is equal to the mutual orbit mean motion. The minimum energy

Table 1
Simulation Parameters

Figure	Object	Primary		Secondary					Mutual Orbit	
		R_p (m)	ρ_p (kg m^{-3})	c (m)	ab (m^2)	a/b	ω_0 (kg m^{-3})	ρ_s (m)	a	e
1	Test	493	1581	190	57,600	1.10	0.53	2618	3300	0.05
3	(1991 VH) ^d	600	1581	190	57,600	1.50	1.07	Various	3300	0.05
4	(1991 VH) ^l	600	1581	190	57,600	1.01	0.17	2618	3300	0.05
5	(1991 VH) ^m	600	1581	190	57,600	1.06	0.42	2618	3300	0.05
7	(1991 VH)	600	1581	190	57,600	1.50	1.07	2618	3300	0.05
8	(2003 YT1)	550	2712	88	11,025	1.30	0.88	3248	3930	0.18
9	(2004 DC)	180	1461	26	900	1.30	0.88	2000	750	0.30
10	(Didymos)	400	1955	65	5625	Various	Various	2252	1180	0.04
10	(2000 DP107)	400	1791	100	22,500	Various	Various	2122	2692	0.03
10	(2002 CE26)	1750	966	100	22,500	Various	Various	1454	4870	0.025
10	(2001 SN263#1)	1300	996	190	52,900	Various	Various	2320	3800	0.016
10	(1994 CC#1)	310	2076	48	3249	Various	Various	8870	1730	0.002
10	(1999 KW4)	659	1970	190	51,076	1.30	0.88	3321	2548	0.0004
10	(1996 FG 3)	850	1300	200	60,025	1.30	0.88	1592	2535	0.07

Notes. Most physical and orbital characteristics of binary and triple NEAs are adopted or derived from Fang & Margot (2012a). Parameters for 1996 FG3 are from Scheirich et al. (2015). Mass and radius uncertainties are $\sim 10\%$ and $\sim 20\%$, respectively. See text for prescription for a , b , and c values. The first column reports the number of the Figure illustrating the corresponding results. “Object” indicates the asteroid name or designation. The next two columns list parameters related to the primary: R_p and ρ_p are the equivalent radius and mass density of the primary. The next five columns describe parameters related to the secondary (assumed to be an ellipsoid with semi-axes a , b , and c). With our choice of simulation parameters (Section 7), it is convenient to tabulate the quantities c , ab , and the elongation a/b . The fourth parameter describing the secondary, ω_0 , is related to the secondary elongation (refer to Section 4 for definition). The fifth parameter is the mass density ρ_s . The last two columns give the initial osculating semimajor axis and eccentricity of the mutual orbit. For testing purposes, we use several modified versions of binary NEA 1991 VH: ^dfor various densities. ^lfor low secondary elongation. ^mfor moderate secondary elongation.

configuration for this system is for the long axis of the secondary to always point toward the primary, such that its instantaneous spin rate is always equal to the mean motion. If the secondary is disturbed from this configuration, its long axis oscillates about the primary–secondary line due to torques exerted by the primary on the elongated secondary. This oscillation is called free libration and its frequency depends on the shape of the secondary and the mutual orbit parameters. Generally, free libration damps out on short timescales due to tidal friction (Murray & Dermott 1999).

If the mutual orbit is eccentric, the secondary exhibits optical and forced librations about the primary–secondary line even if the free libration is damped out. *Optical libration* is the torque-free oscillation of the long axis of a uniformly spinning secondary about the primary–secondary line. This oscillation would occur even in the case of a spherical secondary as the orbital velocity varies over the course of the orbit. We use ϕ to represent the component of α that is due to optical librations. The amplitude of optical libration depends only on the shape of the mutual orbit and is $\sim 2e$, where e is the eccentricity of the mutual orbit (Murray & Dermott 1999). In the case of an elongated secondary, the primary exerts a periodically reversing torque on it due to the misalignment of the secondary long axis from the primary–secondary line, which results in an oscillation of the secondary about uniform rotation called *forced libration*. We use γ to represent the component of α that is due to forced librations. Forced and optical librations have the same frequency (equal to the mean motion). They are in phase if $\omega_0 = \sqrt{3(B-A)/C} < 1$ and 180° out of phase if $\omega_0 > 1$. We use ψ to represent the sum of forced and optical librations, i.e., $\psi = \gamma + \phi$, and ψ_A to represent the libration amplitude.

For most binary NEA systems, a decoupled framework does not accurately capture the system dynamics. Nevertheless, even in the fully coupled problem around an axially symmetric primary, the secondary exhibits libration behavior similar to the free, forced, and optical librations of the decoupled spin problem. There are two modes of libration in the coupled spin–orbit problem, which we call the *relaxed mode* and *excited mode* of libration. The relaxed mode has the same frequency as the orbital frequency, similar to forced + optical libration in the decoupled spin problem. The excited mode of libration has a different frequency that depends on the shape of the secondary. This libration mode is similar to free libration in the decoupled spin problem. By exploring a range of initial conditions, we can minimize the excited-mode librations so that its amplitude is close 0° , leaving the secondary librating in the relaxed mode. The relaxed mode disappears only when the system is in an equilibrium state, i.e., when the mutual orbit is circular and the long axis of the secondary always points toward the primary.

For systems in which the exchange of angular momentum in the system is small, the coupled spin–orbit problem approaches the decoupled problem and the relaxed-mode and excited-mode librations become similar to the forced + optical and free librations, respectively. Because most of our simulations include some amount of spin–orbit coupling, we use the relaxed/excited mode terminology as opposed to the free/forced mode terminology of the decoupled problem.

5. EFFECT OF SPIN–ORBIT COUPLING ON LIBRATION

In this section, we study the effects of spin–orbit coupling on the relaxed-mode libration amplitude of the secondary. Under the assumptions of a fixed orbit around a spherical or point-mass primary, the amplitudes of forced + optical librations (ψ_A) in the decoupled case can be estimated with (e.g.,

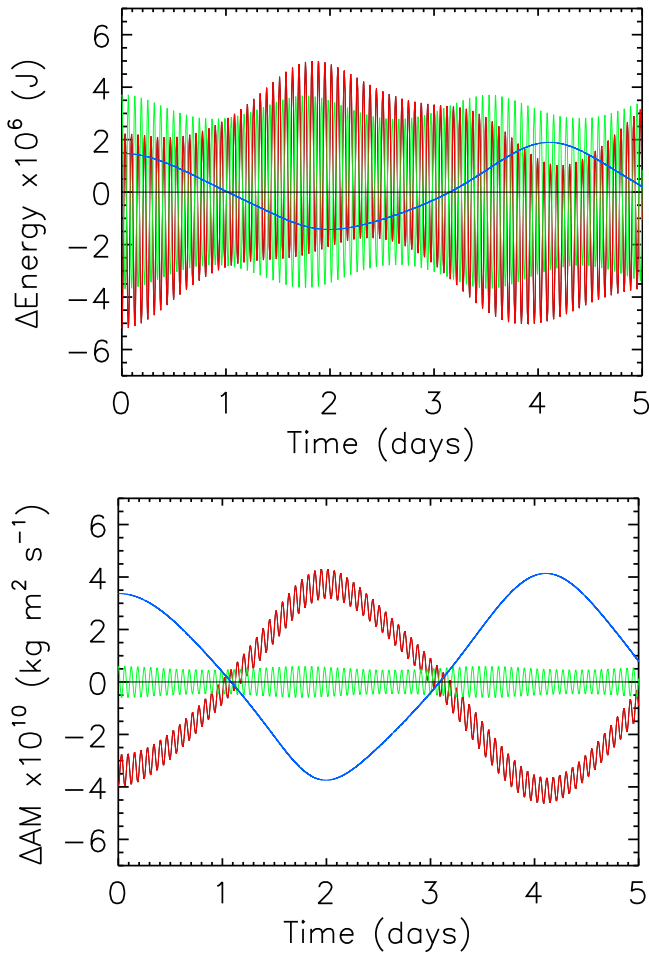


Figure 1. Energy (top) and angular momentum (bottom) variations over the course of 5 days for a typical binary NEA (first entry in Table 1). Lines of different colors represent quantities associated with the mutual orbit (red), the primary spin (green), the secondary spin (blue), and the sum of all three (black).

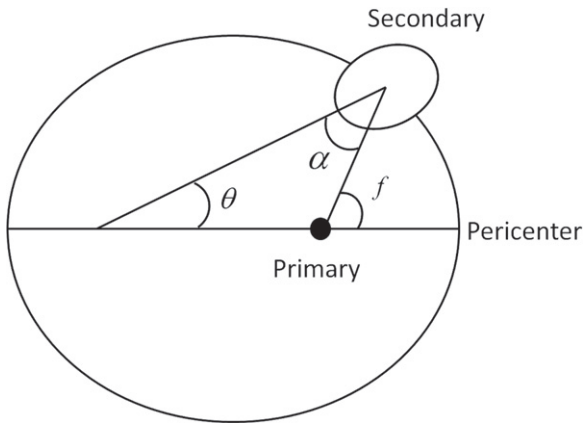


Figure 2. Illustration of the osculating mutual orbit and notation for angles.

Tiscareno et al. 2009):

$$\psi_A = \frac{2e}{\omega_0^2 - 1}, \quad (5)$$

where e is the eccentricity of the mutual orbit and $\omega_0 = \sqrt{3(B-A)/C}$ is the natural frequency of libration of the satellite normalized by the mean motion (n) of the mutual

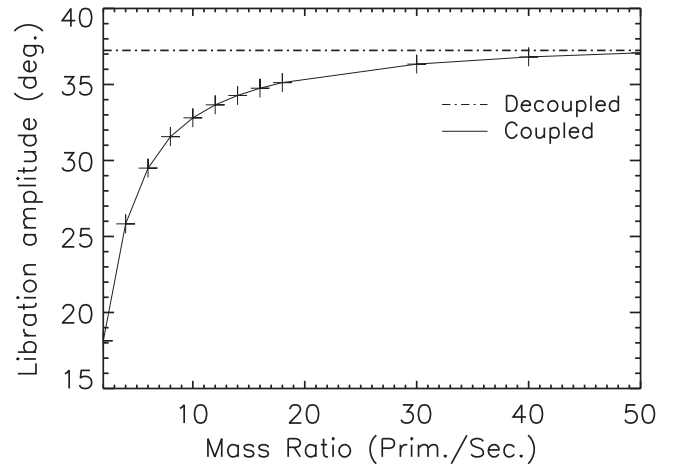


Figure 3. Influence of spin–orbit coupling on relaxed-mode libration amplitude. Plus symbols (connected by a solid line) show amplitudes of relaxed-mode libration as a function of primary-to-secondary mass ratio. Dotted–dashed line shows corresponding analytical estimates of forced + optical libration computed using Equation (5). System parameters for this simulation are based on asteroid 1991 VH and are given in the second row of Table 1. The elongation of the secondary, $alb = 1.5$, corresponds to $\omega_0 = 1.07$.

orbit. In the coupled problem, the amplitude of the librations depends on the primary-to-secondary mass ratio, which we quantify with our fully coupled spin and orbit integrator.

Figure 3 shows results of simulations in which we vary the primary–secondary mass ratio for a binary system based on NEA 1991 VH (row 2 of Table 1, nominal mass ratio ≈ 12). We vary the density of the secondary while keeping other shape parameters constant, and we use initial conditions that make the excited-mode libration amplitude $\sim 0^\circ$. The corresponding analytical estimates (Equation (5)) yield $\psi_A = 37.2^\circ$ for $\omega_0 = 1.07$ and $e = 0.05$. At low values of the primary-to-secondary mass ratio, the libration amplitudes are considerably smaller than the analytical estimate, suggesting that spin–orbit coupling tends to damp libration amplitudes.

6. SURFACE OF SECTION

It is useful to visualize the dynamics with surface of section plots similar to those in Wisdom et al. (1984). At every pericenter passage of the secondary, we plot the angle between the long axis and the line of apsides of the mutual orbit, θ_p , against its time derivative, $\dot{\theta}_p$, normalized by the mean motion, n . In order to identify pericenter passage, we use Keplerian elements to describe the osculating mutual orbit at each time step. These elements vary on timescales shorter than the orbital period because the orbit is not Keplerian.

It is easy to differentiate between regular and chaotic trajectories on surface of section plots: regular trajectories fall on smooth curves, whereas chaotic trajectories fill up an area of the phase space over successive visits (Wisdom et al. 1984). Figure 4 shows different types of trajectories of a slightly elongated secondary in this phase space. The system parameters for this plot are based on radar-derived estimates for NEA 1991 VH (Margot et al. 2008; Naidu et al. 2012) and are given in row 3 of Table 1. The plot looks symmetric about $\theta_p = 90^\circ$ because we use triaxial ellipsoids for the simulations, so $\theta_p = 0^\circ$ is equivalent to $\theta_p = 180^\circ$. Seven trajectories with different initial conditions are shown in this figure. Throughout a simulation, the secondary remains on the trajectory it started

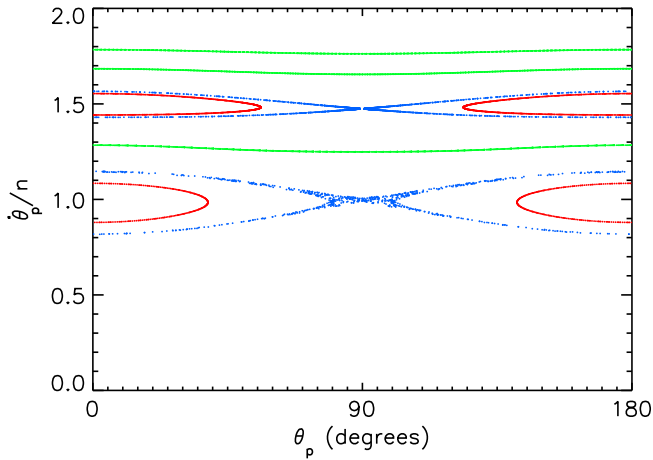


Figure 4. Surface of section plot for a secondary elongation $ab = 1.01$, corresponding to $\omega_0 = 0.17$, and mutual orbit eccentricity $e = 0.05$. Other system parameters are listed in Table 1. Seven trajectories with initial $\dot{\theta}_p/n$ values of 1.08, 1.15, 1.28, 1.55, 1.57, 1.68, and 1.78 are plotted. Initial θ_p values are 0 in all cases. Red, blue, and green colors indicate resonant, chaotic, and non-resonant quasi-periodic trajectories, respectively.

on. The red and green trajectories are regular quasi-periodic, whereas the blue trajectories are chaotic.

On a resonant (red color) trajectory, the secondary librates in a spin-orbit resonance region. For the red trajectory surrounding $\dot{\theta}_p/n = 1.5$, the secondary spins three times for every two orbits, so it is in a 3:2 spin-orbit resonance. Mercury is the only known object in a 3:2 spin-orbit resonance. For the red trajectory surrounding $\dot{\theta}_p/n = 1$, the secondary is in a 1:1 spin-orbit resonance, i.e., it spins synchronously (e.g., the Earth’s Moon). Similar trajectories with islands centered exclusively on $\theta_p = 0^\circ$ and $\theta_p = 180^\circ$ exist near half-integer values of $\dot{\theta}_p/n$ (2, 2.5, 3, etc). The horizontal extent of the trajectory around $\theta_p = 0^\circ$ gives the amplitude of excited-mode libration (equivalent to free libration in the decoupled spin problem). For example, on the red trajectory in the 1:1 resonance region, the secondary has an excited mode libration amplitude of $\sim 37^\circ$. A trajectory with only relaxed-mode libration plots as a point on the y -axis, which we call the *center* of the resonance region (not shown in the figure). The relaxed-mode libration is not detectable in the horizontal dimension of the surface of section plots because we sample the spin state of the secondary at pericenter, where the relaxed-mode libration is always at 0° phase. However, the relaxed-mode libration is detectable in the vertical dimension of the surface of section plots because it contributes to the angular velocity of the secondary at apocenter. The centers of the resonance regions are displaced vertically from their nominal positions in the absence of relaxed-mode libration. These offsets can be seen clearly for relaxed-mode librations with larger amplitudes (Figures 7 and 8). They are strictly due to torques on the permanent deformation of the satellite and are unrelated to the tidally induced pseudo-synchronous rotation described by, e.g., Ferraz-Mello (2013) for nearly spherical satellites on eccentric orbits.

A chaotic (blue color) trajectory marks the boundary of a resonance region and is called a separatrix. On a separatrix the secondary explores the entire range of θ_p values and the trajectory fills up a region of phase space, indicating that the trajectory is chaotic.

Secondary spin rates that are further away from the resonance regions put the secondary on a trajectory similar to one of the non-resonant quasi-periodic (green) trajectories. On these trajectories the secondary is not in a spin-orbit resonance and circulates through all θ_p values in a quasi-periodic manner. These trajectories are called quasi-periodic because they exhibit at least one non-commensurate frequency in addition to the frequency at which the motion is sampled.

Wisdom et al. (1984) assumed that the secondary spin is decoupled from the mutual orbit, a reasonable assumption for the Saturn–Hyperion system because Hyperion has negligible angular momentum compared to the mutual orbit. Under this approximation, they derive the half-widths of the resonance regions (Equation (6), in units of the mean motion) and of the chaotic separatrix surrounding the 1:1 spin-orbit resonance (Equation (7), in the energy domain):

$$\frac{1}{2}\text{RW} = \omega_0 \sqrt{|H(p, e)|}; \quad (6)$$

$$\frac{1}{2}\text{SW} = \frac{\Delta E}{E_0} \approx \frac{14\pi e}{\omega_0^3} e^{-(\pi/2\omega_0)}. \quad (7)$$

Here, H are functions tabulated in Cayley (1861) and p is the spin-orbit resonance ratio, e.g., $p = 3/2$ for a 3:2 spin-orbit resonance. ΔE represents energy variations on the chaotic separatrix and E_0 comes from the first integral of the averaged equation of motion of libration (Wisdom et al. 1984). It is the energy at which the libration angle begins to circulate:

$$E_0 = \frac{1}{4} n^2 \omega_0^2 C, \quad (8)$$

where C is the moment of inertia about the spin axis. In the averaged equation of motion, the higher frequency terms that give rise to chaos are ignored, so the separatrix is regular.

The width of the resonance and of the chaotic regions grow larger with ω_0 and e . For large enough values, neighboring resonance regions overlap, resulting in a large chaotic zone surrounding the overlapping resonances. The resonance overlap criterion for the 1:1 and 3:2 spin-orbit resonances is given by (Wisdom et al. 1984):

$$\omega_0^{\text{RO}} = \frac{1}{2 + \sqrt{14}e}. \quad (9)$$

Overlap occurs when $\omega_0 > \omega_0^{\text{RO}}$.

These equations were derived under the assumption that the secondary spin has no feedback on the mutual orbit, and we investigate whether the analytical formulation (Equation (9)) matches the results of our coupled integrator. For a system based on 1991 VH (Table 1), we varied the elongation in steps of 0.01 and determined when resonance overlap occurred. We find that it does not occur for $ab = 1.03$ ($\omega_0 = 0.30$) but that it does occur for $ab \geq 1.04$ ($\omega_0 \geq 0.34$). The analytical estimate, which does not take the width of the separatrix into account, places the onset of chaos at $\omega_0^{\text{RO}} = 0.35$ for $e = 0.05$. The small difference between the analytical and numerical estimates for the onset of chaos suggests that Equation (9) provides a reasonable approximation even in the presence of spin-orbit coupling. In subsequent sections, we will confirm this finding by providing values for both estimates for a variety of orbital eccentricities. Note that Wisdom et al. (1984) also observed a small difference between analytical and numerical estimates, even in the fully decoupled case. To illustrate resonance

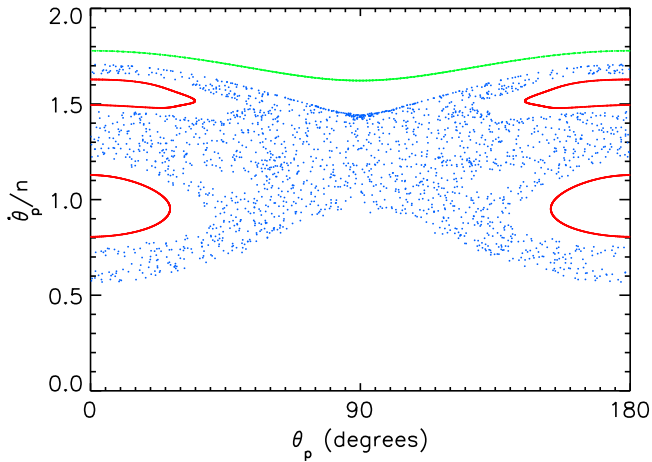


Figure 5. Surface of section plot illustrating the partial overlap of the 1:1 and 3:2 spin-orbit resonances for a secondary elongation $a/b = 1.06$, corresponding to $\omega_0 = 0.42$, and a mutual orbit eccentricity $e = 0.05$. Other system parameters are given in Table 1. Four trajectories with initial $\dot{\theta}_p/n$ values of 1.13, 1.63, 1.70, and 1.78 are plotted. Initial θ_p values are 0 in all cases. Color scheme as in Figure 4.

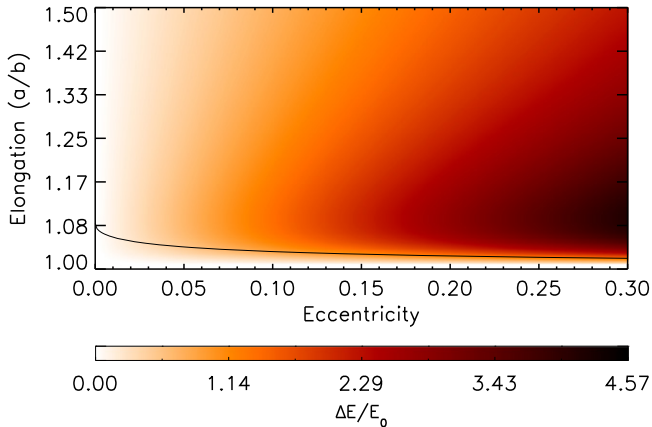


Figure 6. Contour plot showing the half-width of the chaotic separatrix $\Delta E/E_0$ as a function of a/b and e (Equation (7)). According to the resonance overlap criterion of Equation (9), overlap will occur in systems that lie above the solid line.

overlap, we generate a surface of section for a value of $a/b = 1.06$ and $e = 0.05$ such that $\omega_0 = 0.42 > \omega_0^{\text{RO}} = 0.35$ (Figure 5). The overlap wipes out the non-resonant quasi-periodic trajectories between the overlapping resonances and results in smaller 1:1 and 3:2 spin-orbit resonance regions and a large chaotic zone surrounding the resonances.

Substituting $e = 0$ in Equation (9) yields $\omega_0^{\text{RO}} = 0.5$ which corresponds to $a/b \approx 1.09$. This value is low compared to typical elongations observed in asteroids (e.g., Hudson & Ostro 1995; Hudson et al. 2000; Naidu et al. 2013). The secondary of 1999 KW4 has an elongation of 1.3 (Ostro et al. 2006). This suggests that resonance overlaps are quite likely to happen in binary NEAs. However, for small eccentricities the width of the chaotic separatrix remains small as dictated by Equation (7), so resonance overlaps do not result in large chaotic regions. The resonance overlap threshold of a/b as a function of e (Equation (9)) and the width of the chaotic separatrix ($\Delta E/E_0$) as a function of e and a/b (Equation (7)) are plotted in Figure 6. The figure illustrates that the size of the chaotic zone increases with eccentricity.

In the next section, we examine the surface of section plots for well-characterized binary and triple systems.

7. WELL-CHARACTERIZED BINARY AND TRIPLE NEA SYSTEMS

We simulate the spins and orbits of well-characterized binaries and triples listed in Fang & Margot (2012a), which includes both *synchronous* ($\langle \dot{\theta}/n \rangle = 1$) and *asynchronous* ($\langle \dot{\theta}/n \rangle \neq 1$) systems, where $\langle \cdot \rangle$ indicates values averaged over one orbit. We use our integrator to determine the minimum elongation at which resonance overlap occurs and, for synchronous satellites, the amplitude of relaxed-mode libration. We also plot surfaces of section for each system to examine the variety of dynamical regimes. When satellite elongations are not known, we assume a value of 1.3, which corresponds to that of the 1999 KW4 satellite. Equivalent radii for the components and mutual orbital parameters are obtained from Fang & Margot (2012a), unless otherwise indicated.

In all cases, we assume the primaries to be spherical and the secondaries to be triaxial ellipsoids. We need a prescription for choosing the axial dimensions such that they conform to the radius and mass of the secondary described in the literature. a and b are chosen to satisfy two conditions: (1) $a \times b = R_s^2$, where R_s is the radius of the secondary, and (2) a/b equals the desired elongation. c is chosen in a way that ensures $A < B < C$. The choice of c is not crucial because the dynamics are mostly sensitive to the value of $\omega_0 = \sqrt{3(B-A)/C}$ which, for a triaxial ellipsoid, is equal to $\sqrt{3(a^2 - b^2)/(a^2 + b^2)}$. The adopted density of the satellite is based on the observed mass of the satellite and on the volume of the triaxial ellipsoid. Because the choice of c is arbitrary, the densities used in the simulations are not identical to the nominal densities, but the masses used in the simulations do conform to the nominal masses. We verified the robustness of our results by running simulations with up to 20% changes in the values of c and found no appreciable difference in the surface of section plots.

7.1. 1991 VH

As mentioned in Section 6, the overlap of the 1:1 and 3:2 spin-orbit resonances of the 1991 VH secondary happens for $a/b > 1.04$. Radar images show that its equatorial elongation is about 1.5 (Naidu et al. 2012). Figure 7 shows a surface of section plot for $e = 0.05$ and $a/b = 1.5$ (other parameters are listed in Table 1). At these values, the chaotic zone completely wipes out the 3:2 spin-orbit resonance but a large stable 1:1 spin-orbit resonance region still exists. The center of the synchronous region (as defined in Section 6) is on the y -axis in Figure 7, in the region bounded by the smaller red trajectory close to $\dot{\theta}_p/n = 0.5$. It is shifted down from $\dot{\theta}_p/n = 1$ due to relaxed-mode libration which makes a non-zero contribution to $\dot{\theta}$ at pericenter. We measure the relaxed-mode libration amplitude at the resonance center to be about 35° .

The synchronous region is surrounded by a chaotic zone. This has implications for synchronous capture that are discussed in Section 8. If the secondary gets captured in the synchronous region, tides are expected to damp the excited-mode libration of the secondary, driving its trajectory toward the center of the synchronous region, where it exhibits only relaxed-mode libration. Since the spin is coupled to the orbit, energy removed from the secondary spin will gradually change the orbit, the surface of section map, and the relaxed-mode

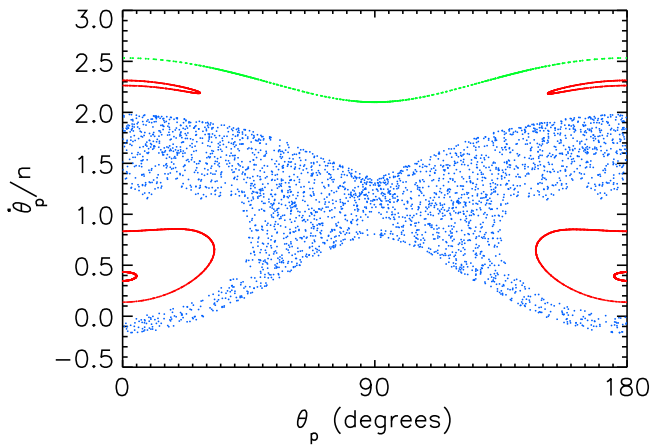


Figure 7. Surface of section plot for the 1991 VH secondary using the radar-derived secondary elongation $alb = 1.5$, corresponding to $\omega_0 = 1.07$, and the mutual orbit eccentricity $e = 0.05$. Other system parameters are given in Table 1. Five trajectories with initial $\dot{\theta}_p/n$ values of 0.43, 0.83, 1.63, 2.31, and 2.53 are plotted. Initial θ_p values are 0 in all cases. Color scheme is the same as in Figure 4.

libration amplitude and frequency. Throughout this evolution, the secondary remains in the same dynamical regime close to the center of the synchronous region. The next higher order stable resonance is the 2:1 resonance, however probability of capture into this resonance is low ($\sim 10^{-3}$ using equation (5.110) of Murray & Dermott 1999). Similar to the synchronous region, the 2:1 resonance region is shifted vertically from $\dot{\theta}_p/n = 2$. The shift in this case is upwards because the instantaneous satellite spin rate at pericenter is greater than its orbit-averaged value of $2n$.

Preliminary measurements of the Doppler extents (or bandwidths) of the secondary in radar images (Margot et al. 2008; Naidu et al. 2012) are consistent with chaotic behavior, but because of the large amplitude libration at the resonance center and corresponding spin rate variations (Section 8.2), we cannot entirely rule out the possibility of synchronous spin.

7.2. 2003 YTI

This system’s component sizes are $R_p \approx 550$ m and $R_s \approx 105$ m, so the primary is similar to that of 1991 VH but the secondary is a few times smaller. The orbit ($a/R_p \sim 7$) is somewhat wider than that of 1991 VH ($a/R_p \sim 5.5$), and it is also more eccentric ($e = 0.18$ versus $e = 0.05$). The smaller secondary and wider mutual orbit mean that spin and orbit are less coupled in this system than in 1991 VH. Substituting $e = 0.18$ in Equation (9), we get a theoretical threshold for resonance overlap $\omega_0^{\text{RO}} = 0.30$, which corresponds to $alb = 1.03$. Using our simulations we find that the resonance overlap threshold lies between $\omega_0 = 0.24$ ($alb = 1.02$) and $\omega_0 = 0.30$ ($alb = 1.03$). The elongation of the satellite is unknown. For our simulations (Figure 8), we chose an elongation of 1.3.

The 1:1 spin-orbit resonance region is not as prominent in this plot as it is in Figure 7 due to the higher eccentricity. Despite the higher eccentricity, the y -axis location of the synchronous region center is similar to that of 1991 VH, because of the smaller satellite elongation. The chaotic region is much bigger than that of 1991 VH and extends to $\dot{\theta}_p/n \approx 3$. The first higher order stable resonance is the 5:2 spin-orbit

resonance. This resonance region is shifted upwards from $\dot{\theta}_p/n = 2.5$, similar to the upward shift of the 2:1 resonance region of 1991 VH. The amplitude of the relaxed-mode libration measured at the center of the synchronous region is about 45° .

7.3. 2004 DC

2004 DC has the smallest primary ($R_p \approx 180$ m), secondary ($R_s \approx 30$ m), and mutual orbit semimajor axis (750 m) in our sample, but it has the most eccentric mutual orbit ($e \approx 0.3$) (Table 1). The resonance overlap criterion (Equation 9) gives $\omega_0^{\text{RO}} = 0.25$, which corresponds to an elongation of $alb = 1.02$. Using our simulations we find that the resonance overlap threshold lies between $alb = 1.01$ ($\omega_0 = 0.17$) and 1.02 ($\omega_0 = 0.24$), roughly consistent with the analytical estimate. The shape of the secondary is not known, however its appearance in the radar images suggest that $alb \leq 1.3$ (Patrick Taylor 2014, private communication). Figure 9 shows the surface of section plot for a secondary having an elongation of 1.3 (system parameters in Table 1). The chaotic region is so large that even the 1:1 resonance region disappears and the lowest-order stable resonance region is the 4:1 spin-orbit resonance. In fact the synchronous island is absent for all values of satellite elongations ≥ 1.1 .

7.4. Synchronous Satellites

Radar data show that the satellites of 2000 DP107, 2002 CE26, 2001 SN263 (Gamma), 1999 KW4, and 1994 CC (Beta) are synchronous (Margot et al. 2002; Ostro et al. 2006; Shepard et al. 2006; Nolan et al. 2008; Brozović et al. 2011, respectively). Didymos may also be synchronous (Benner et al. 2010); for our purposes we assume that it is. Scheirich et al. (2015) found that 1996 FG3 is synchronous. We use radar-derived mutual orbital parameters, component radii, and component masses for simulating these systems. These parameters are given in Table 1. For satellites whose elongations are not well known, we perform simulations using $alb = 1.01, 1.05, 1.1, 1.2,$ and 1.3. Each simulation is performed with initial conditions that put the trajectory at the center of the synchronous island. We identify the center of the synchronous island by varying the values of initial $\dot{\theta}$ until the horizontal extent of the trajectory on the surface of section becomes ~ 0 . As mentioned in Section 7.1, the excited-mode libration amplitude is zero at the center of the synchronous island, which is what is expected for a tidally evolved satellite. In this case, the satellite exhibits only the relaxed-mode libration, which we measure as the angle between the long axis of the secondary and the line joining the primary and secondary centers of masses (in the decoupled terminology, this is the optical + forced libration). The libration amplitudes, i.e., the maximum values of the libration angles, are plotted as a function of elongation in Figure 10. The analytical estimates of the libration amplitudes, assuming the decoupled spin-orbit problem, are given by Equation (5).

Since shape and spin state modeling are tied to each other (e.g., Ostro et al. 2006; Naidu et al. 2013), calculations such as those shown in Figure 10 are useful for shape modeling of asteroid satellites. These estimates are also useful for modeling binary YORP torques (Ćuk & Burns 2005) on synchronous satellites. If a system exhibits excited-mode libration in addition to the relaxed-mode libration, the two librations will

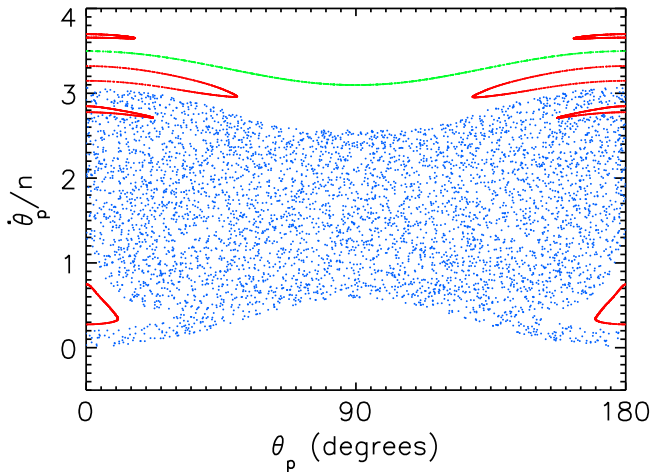


Figure 8. Surface of section plot for the 2003 YT1 secondary assuming the secondary elongation $ab = 1.3$, corresponding to $\omega_0 = 0.88$, and the mutual orbit eccentricity $e = 0.18$. Other system parameters are given in Table 1. Six trajectories with initial $\dot{\theta}_p/n$ values of 0.75, 1.29, 2.85, 3.15, 3.5, and 3.69 are plotted. Initial θ_p values are 0 in all cases. Color scheme is the same as in Figure 4.

add up and create a beating pattern. Because the amplitudes and frequencies of excited-mode libration can span a wide range of values, 3D reconstruction and binary YORP modeling of dynamically excited satellites is complicated.

8. IMPLICATIONS

8.1. Presence of Chaotic Regions and Synchronous Capture

In Section 7, we showed that resonance overlap is likely to occur for asynchronous satellites in our sample and that large chaotic zones are expected in their phase spaces. This behavior can be expected in other, similar systems. Let us consider the evolution of a satellite formed with a high initial spin rate such that its trajectory in phase space is in or above the chaotic zone, the situation expected for most satellites in the formation model of Jacobson & Scheeres (2011a). It is possible for YORP to increase the spin rate of the satellite, but we focus on the spin-down evolution under the influence of tidal and YORP forces. Satellites that start above the chaotic region will most likely encounter the chaotic zone on their way to the 1:1 spin-orbit resonance region. In the chaotic zone, the satellite is acted upon by tides, YORP, and torques on its permanent shape, which cause the chaotic spin. Since the spin of the satellite is coupled to the mutual orbit, angular momentum removed or added to the secondary spin by tides and YORP will also affect the mutual orbit and cause the surface of section map of the secondary to vary. However, for binary NEAs, the angular momentum of the mutual orbit is much greater than that of the secondary spin, so the effect is expected to be small. We neglect this effect for the following discussion and assume the surface of section map to be roughly constant during the evolution of the secondary spin in the chaotic zone.

If the chaotic separatrix around the 1:1 spin-orbit resonance region is extremely thin, as is the case for satellites having almost spherical shapes, then the torques on the permanent shape will be small, allowing tides or YORP to easily drive the satellite spin across the separatrix and into the synchronous region. For satellites having larger chaotic zones, like the asynchronous satellites in Section 7, tides or YORP cannot

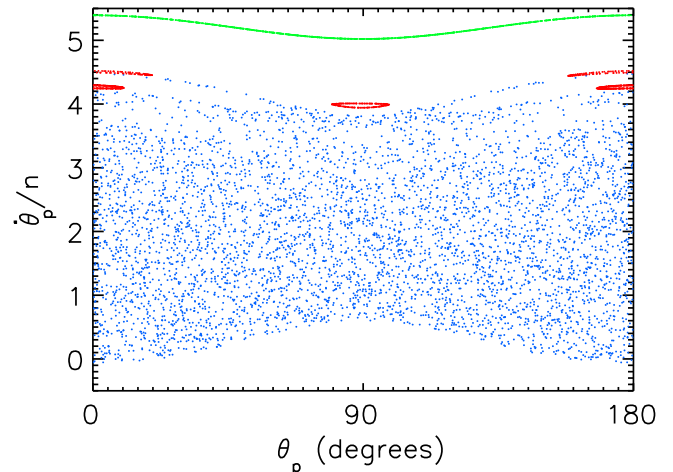


Figure 9. Surface of section plot for the 2004 DC secondary assuming the secondary elongation $ab = 1.3$, corresponding to $\omega_0 = 0.88$, and the mutual orbit eccentricity $e = 0.3$. Other system parameters are given in Table 1. Four trajectories with initial $\dot{\theta}_p/n$ values of 1.39, 4.29, 4.49, and 5.39 are plotted. Initial θ_p values are 0 in all cases. Color scheme is the same as in Figure 4.

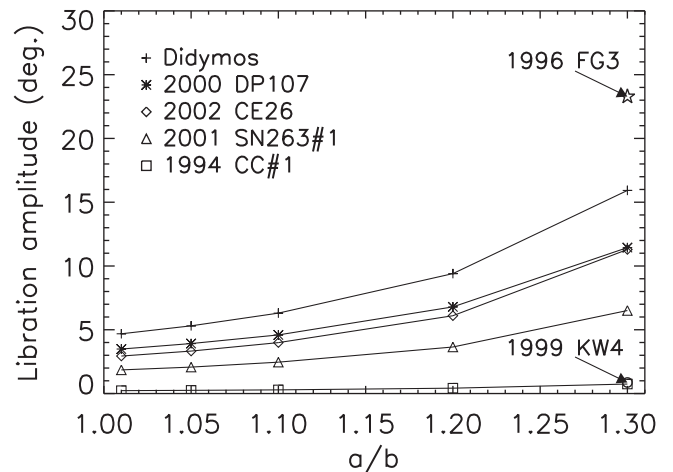


Figure 10. Numerical estimates of relaxed-mode libration amplitude as a function of satellite elongation for synchronous satellites among well-characterized binary and triple systems. For 1999 KW4 and 1996 FG3, we plot single points corresponding to the known elongations of the satellites. The libration amplitude of 1996 FG3 is an upper limit based on an eccentricity of 0.07.

simply sweep the satellite across the chaotic region because torques on the permanent shape can increase as well as decrease the spin rate of the satellite in a random manner. The synchronous capture process is essentially stochastic in nature. For capture to occur, the satellite has to spend enough time near the boundary of the synchronous region for tides or YORP to torque the satellite into resonance. Such a process was discussed by Wisdom et al. (1984). The details of this capture process are not known and are difficult to model, however the probability of this happening will depend on the relative magnitude of $\Delta E/E_0$ compared to the energy dissipated due to tides ($\delta E_{\text{tides}}/E_0$) or YORP ($\delta E_{\text{YORP}}/E_0$).

Simulations and Equation (7) show that values of chaotic spin energy variations ($\Delta E/E_0$) for the asynchronous satellites are within an order of magnitude of 1. We estimate the

magnitude of tidal dissipation in one orbit using the following Equation from Murray & Dermott (1999):

$$\delta E_{\text{tides}} = \pi \frac{3}{2} \frac{k_2 n^4}{Q G} R_s^5. \quad (10)$$

Here k_2 is the Love number, Q is the tidal dissipation factor, n is the mean motion, G is the gravitational constant, and R_s is the radius of the secondary. We approximate energy dissipation due to YORP in one orbit by multiplying the YORP torque given in Steinberg & Sari (2011) by the satellite rotation over one orbit, 4π assuming two satellite rotations per orbit:

$$\delta E_{\text{YORP}} = \frac{2\pi R_s^3 L_{\odot} f_Y}{3cd^2 \sqrt{1 - e_{\odot}^2}}. \quad (11)$$

Here L_{\odot} is the solar luminosity, f_Y is the YORP torque efficiency, c is the speed of light, d and e_{\odot} are the semimajor axis and eccentricity of the heliocentric orbit, respectively. In order to compare the tidal and YORP energy dissipation with $\Delta E/E_0$, we normalize δE_{tides} and δE_{YORP} using E_0 from Equation 8.

For computing δE_{tides} we assume $Q = 100$ and estimate k_2 values using three different models. In the rubble pile model of Goldreich & Sari (2009), $k_2 = 10^{-5} R_s$, where R_s is in km. Using the system parameters from Table 1, we determine $\delta E_{\text{tides}}/E_0$ for all the asynchronous satellites to be between 10^{-9} and 10^{-8} . Assuming the monolith model of Goldreich & Sari (2009) for the secondary yields lower values of δE_{tides} because a monolith is more rigid than a rubble pile of the same size and has a lower value of k_2 . Jacobson & Scheeres (2011b) derived a different relation between Love number and radius, $k_2 = 2.5 \times 10^{-5} R_s^{-1}$, by assuming that orbits of observed synchronous asteroid satellites are in an equilibrium state such that tidal torques balance binary YORP torques. Substituting k_2 values from this relation in Equation (10) yields $\delta E_{\text{tides}}/E_0$ between 10^{-7} and 10^{-5} . We compute δE_{YORP} by assuming $f_Y = 5 \times 10^{-4}$, the estimated value for asteroid YORP (Lowry et al. 2007; Taylor et al. 2007). $\delta E_{\text{YORP}}/E_0$ values for 1991 VH, 2003 YT1, and 2004 DC are 5×10^{-7} , 3×10^{-6} , and 2×10^{-5} , respectively.

Unknown values of Q , k_2 , and f_Y introduce uncertainties of a few orders of magnitude in δE_{tides} and δE_{YORP} but these energy dissipation values are several orders of magnitudes smaller than $\Delta E/E_0$, suggesting that chaotic variations in energy dominate tidal and YORP dissipations in these systems. This may substantially delay spin synchronization and, therefore, BYORP-type evolution.

If the timescale for synchronous capture is long, then tides may damp the mutual orbit eccentricity significantly before spin synchronization. This will reduce the size of the chaotic zone as dictated by Equation (7) and make it easier for tides or YORP to torque the secondary into the synchronous region. Tidal damping of eccentricity is not a very effective process and timescales may be quite long. Fang & Margot (2012a) estimated timescales in the range 10^7 – 10^{10} years for the asynchronous satellites, but these may be in error because the underlying formalism by Goldreich (1963) assumes synchronous rotators. It is likely that energy dissipates faster in the case of satellites that are torqued and tidally deformed in a chaotic manner, but the nature and characteristic timescale of the eccentricity evolution remain poorly known. Complicating the picture is the fact that other mechanisms such as solar perturbations (Scheeres et al. 2006) or planetary flybys

(Farinella 1992; Fang & Margot 2012b) may also be effective at damping or exciting eccentricities. Although there is uncertainty related to the eccentricity-damping timescale, BYORP-type evolution cannot take place until the spin period is synchronized to the orbital period. Asteroid binaries may enjoy extended lives because their chaotically spinning secondaries prevent BYORP evolution.

8.2. Interpretation of Observational Data

Our results have implications for radar and light curve data interpretation. In radar observations (images and spectra), the Doppler extent (or bandwidth) of an object is proportional to its apparent, instantaneous spin rate (inversely proportional to its spin period). Light curves show variations in the object's brightness as it spins. If the object is spinning at a constant rate, the brightness variations will be approximately periodic. The primary periodicity in the light curve (e.g., Pravec et al. 2006) is often used as a proxy for the object's spin rate, even though the signal is affected by changes in relative positions between the Sun, the object, and the observer. We showed in Section 7 that asteroid satellite spin rates can be time-variable. When the light curve data are of sufficient quality and when $R_s/R_p \gtrsim 0.2$, it is sometimes possible to distinguish the signal of the secondary from that of the primary. In radar data, where the secondary is typically easily detectable, the spinning satellite will exhibit approximately periodic bandwidth variations. However, in both cases, a variable spin rate severely complicates the analysis. Understanding the time-varying nature of the satellite spin is important when analyzing radar and light curve data.

Figure 11 shows spin rate as a function of time for four trajectories of 1991 VH. The top panel shows a trajectory at the center of the synchronous island. Even though it would plot as a point on a surface of section, the satellite spin rate exhibits a large oscillation at the orbital rate with an amplitude slightly greater than the mean motion, n . As mentioned in Section 6, this oscillation is the relaxed-mode libration of the satellite.

The second panel in Figure 11 shows a chaotic trajectory. The spin rate variations span a similar, but slightly larger, range of values than that in the synchronous case. If observations (radar or photometric) were sparse, it would be difficult or even impossible to ascertain whether a trajectory was periodic or chaotic. With a sufficient number of data points sampled at a sufficiently fast cadence, one could examine the distribution of spin rate values to identify the type of trajectory, as the distributions for resonant and chaotic trajectories are different. Spin rate variations on the synchronous trajectory resemble a sinusoid, so the distribution of spin rates looks approximately bimodal. The spin rate distribution of the satellite in the chaotic region cannot be generalized and depends on specific system parameters.

The third and fourth panels show the 3:2 resonant trajectory (red) and the quasi-periodic (green) trajectory of Figure 7, respectively. In these cases, the variations are much smaller than the previous two trajectories. These rotational regimes are easier to identify because large-scale chaotic variations are not present.

In radar data analysis, modeling the spin state and shape of objects are tied to each other (e.g., Ostro et al. 2006; Naidu et al. 2013). Incorrect spin state assumptions may yield incorrect shape models. Our results indicate that in some cases it will be impossible to identify the spin state of the satellite,

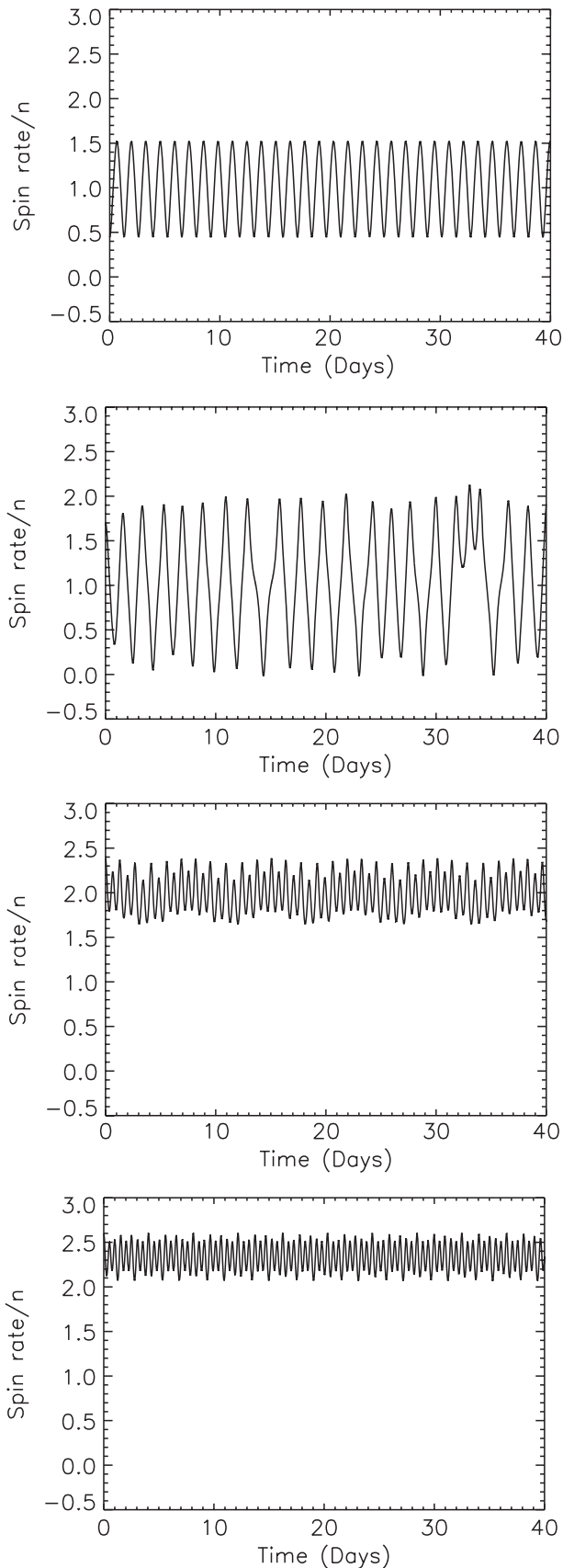


Figure 11. Satellite spin rate variations for four possible trajectories of 1991 VH. From top to bottom, the initial values of satellite spin rate, normalized by n , are 0.45, 1.70, 2.38, 2.60.

whereas in other cases an appropriate rotational model will provide a good fit to the data. A simple model of uniform rotation may not be sufficient, as libration amplitudes can cause displacements that exceed the image resolution. We recommend using a model that includes librations for the 3D reconstruction of asteroid satellites with even moderate eccentricity and elongation.

9. CONCLUSIONS

We examined the rotational regimes of asteroid satellites using surfaces of section. The trajectories can be broadly classified as resonant, non-resonant quasi-periodic, and chaotic. In order to identify the specific type of spin behavior, a dense time sampling of the satellite spin state is necessary (Section 8.2), however such data sets are seldom available. Even densely sampled light curves, for instance, do not yield measurements of the instantaneous spin state due to the necessity of observing ~ 1 full period to estimate the spin period. In Section 8.2, we showed that even synchronous satellites can undergo large variations in spin rates, potentially masquerading as asynchronous satellites. Careful analysis of the data along with coupled spin-orbit simulations can be used to correctly identify the spin behavior. Identifying the spin configurations is essential for obtaining accurate physical models of the satellites.

The spin configurations of satellites play a crucial role in the secular evolution of binary/triple systems under the influence of forces such as tides and binary YORP. For example, the binary YORP torque acts only on satellites whose spin periods are integer multiples of their orbital periods (Čuk & Burns 2005) and some estimates suggest that this torque could disrupt binary systems in just a few tens of thousands of years (Čuk & Nesvorný 2010; McMahon & Scheeres 2010). Thus understanding the process of spin synchronization is essential for understanding the evolution of binaries. In Section 8.1, we showed that satellites may have significantly longer spin synchronization timescales than those estimated by considering tidal and/or YORP forces only. This would increase the fraction of asynchronous binaries in the observed population beyond what one would expect on the basis of tidal despinning timescales. The corresponding delay in the onset of binary YORP implies that the lifetimes of binary asteroids can be significantly longer than the few tens of thousands of years suggested by binary YORP models.

10. FUTURE WORK

We examined the results of spin-orbit coupling in the planar case. However, Wisdom et al. (1984), using 3D simulations, showed that seemingly stable configurations in planar simulations can be attitude unstable. Future work will involve studying inclined/oblique binary systems in order to test the attitude stability of satellites in various regions of phase space. Our integrator can also be used for studying the secular evolution of binary asteroids. This will require implementation of radiation pressure and tidal forces.

We thank Jack Wisdom, Dan Scheeres, Jay McMahon, and Seth Jacobson for useful discussions, and the anonymous reviewer for excellent suggestions. This material is based upon

work supported by the National Science Foundation under Grant No. AST-1211581.

REFERENCES

- Ashenberg, J. 2007, *CeMDA*, **99**, 149
- Benner, L. A. M., Margot, J., Nolan, M. C., et al. 2010, *BAAS*, **42**, 1056
- Boué, G., & Laskar, J. 2009, *Icar*, **201**, 750
- Brozović, M., Benner, L. A. M., Taylor, P. A., et al. 2011, *Icar*, **216**, 216
- Cash, J. R., & Karp, A. H. 1990, *ACM Trans. Math. Softw.*, **16**, 201
- Cayley, A. 1861, *MmRAS*, **29**, 191
- Čuk, M., & Burns, J. A. 2005, *Icar*, **176**, 418
- Čuk, M., & Nesvorný, D. 2010, *Icar*, **207**, 732
- Fahnestock, E. G., & Scheeres, D. J. 2006, *CeMDA*, **96**, 317
- Fahnestock, E. G., & Scheeres, D. J. 2008, *Icar*, **194**, 410
- Fang, J., & Margot, J.-L. 2012a, *AJ*, **143**, 24
- Fang, J., & Margot, J. L. 2012b, *AJ*, **143**, 25
- Farinella, P. 1992, *Icar*, **96**, 284
- Ferraz-Mello, S. 2013, *CeMDA*, **116**, 109
- Goldreich, P. 1963, *MNRAS*, **126**, 257
- Goldreich, P., & Sari, R. 2009, *ApJ*, **691**, 54
- Hudson, R. S., & Ostro, S. J. 1995, *Sci*, **270**, 84
- Hudson, R. S., Ostro, S. J., Jurgens, R. F., et al. 2000, *Icar*, **148**, 37
- Jacobson, S. A., & Scheeres, D. J. 2011a, *Icar*, **214**, 161
- Jacobson, S. A., & Scheeres, D. J. 2011b, *ApJL*, **736**, L19
- Jacobson, S. A., Scheeres, D. J., & McMahon, J. 2014, *ApJ*, **780**, 60
- Lowry, S. C., Fitzsimmons, A., Pravec, P., et al. 2007, *Sci*, **316**, 272
- Maciejewski, A. J. 1995, *CeMDA*, **63**, 1
- Margot, J. L., Nolan, M. C., Benner, L. A. M., et al. 2002, *Sci*, **296**, 1445
- Margot, J. L., Taylor, P. A., Nolan, M. C., et al. 2008, *BAAS*, **40**, 433
- McMahon, J., & Scheeres, D. 2010, *Icar*, **209**, 494
- McMahon, J. W., & Scheeres, D. J. 2013, *CeMDA*, **115**, 365
- Murray, C. D., & Dermott, S. F. 1999, *Solar System Dynamics* (Cambridge: Cambridge Univ. Press)
- Naidu, S. P., Margot, J. L., Busch, M. W., et al. 2012, in *AAS/Division of Dynamical Astronomy Meeting 43*, 07.07
- Naidu, S. P., Margot, J. L., Busch, M. W., et al. 2013, *Icar*, **226**, 323
- Nolan, M. C., Howell, E. S., Becker, T. M., et al. 2008, *BAAS*, **40**, 432
- Ostro, S. J., Margot, J.-L., Benner, L. A. M., et al. 2006, *Sci*, **314**, 1276
- Pravec, P., Wolf, M., & Šarounová, L. 1999, in *IAU Coll. 173, Evolution and Source Regions of Asteroids and Comets*, ed. J. Svoren, E. M. Pittich, & H. Rickman, (Cambridge: Cambridge Univ. Press), 159
- Pravec, P., Scheirich, P., Kušnirák, P., et al. 2006, *Icar*, **181**, 63
- Press, W. H., Teukolsky, S. A., Vetterling, W. T., & Flannery, B. P. 1992, *Numerical Recipes in C: The Art of Scientific Computing* (2nd ed.; New York: Cambridge Univ. Press)
- Rubincam, D. P. 2000, *Icar*, **148**, 2
- Scheeres, D. J., Fahnestock, E. G., Ostro, S. J., et al. 2006, *Sci*, **314**, 1280
- Scheirich, P., Pravec, P., Jacobson, S. A., et al. 2015, *Icar*, **245**, 56
- Shepard, M. K., Margot, J.-L., Magri, C., et al. 2006, *Icar*, **184**, 198
- Steinberg, E., & Sari, R. 2011, *AJ*, **141**, 55
- Taylor, P. A., Margot, J.-L., Vokrouhlický, D., et al. 2007, *Sci*, **316**, 274
- Tiscareno, M. S., Thomas, P. C., & Burns, J. A. 2009, *Icar*, **204**, 254
- Wisdom, J., Peale, S. J., & Mignard, F. 1984, *Icar*, **58**, 137